

# Autonomous Robotic Drilling System for Mice Cranial Window Creation

Enduo Zhao, Murilo M. Marinho, and Kanako Harada

**Abstract**—Robotic assistance for experimental manipulation in the life sciences is expected to enable favorable outcomes, regardless of the skill of the scientist. Experimental specimens in the life sciences are subject to individual variability hence require intricate algorithms for successful autonomous robotic control. As a use case, we are studying the creation of cranial windows in mice. This operation requires the removal of an 8-mm-circular patch of the skull, which is approximately 300  $\mu\text{m}$  thick, but the shape and thickness of the mouse skull significantly varies depending on the strain of mouse, sex, and age. In this work, we propose an autonomous robotic drilling method with no offline planning, consisting of a trajectory planning block with execution-time feedback with completion level recognition based on image and force information. The force information allows for completion-level resolution to increase 10 fold. We evaluate the proposed method in two ways. First, in an eggshell drilling task and achieved a success rate of 95% and average drilling time of 7.1 min out of 20 trials. Second, in *postmortem* mice and with a success rate of 70% and average drilling time of 9.3 min out of 20 trials.

**Index Terms**—Multi-Arm Robotic Platform, Cranial Window Creation, Multi-sensor Fusion.

## I. INTRODUCTION

A cranial window is a transparent observation window carefully made in the skull of a mouse, providing direct visualization and access to the brain for experimental purposes. For example, to observe human organoids that are introduced into the mouse brain [2]. Cranial window creation involves using a microdrill under a microscope to extract an 8 mm circular section of the mouse skull, which is then replaced with a cover glass. Cranial window procedures are crucial for advancing our understanding of the human cell growth and developing strategies for diagnosing, treating, and preventing neurological disorders. However, the small size and delicate nature of mouse skulls increase the risk of damaging critical structures during the procedure. Additionally, variability in skull thickness and density complicates the operation. These compound to difficulties and experimental complexity given that any damage to the underlying brain tissue results in a catastrophic failure.

This work was supported by JST Moonshot R&D JPMJMS2033.

(Corresponding author: Murilo M. Marinho)

Enduo Zhao is with the Department of Mechanical Engineering, the University of Tokyo, Tokyo, Japan. Email: endowzhao1996@g.ecc.u-tokyo.ac.jp.

Murilo M. Marinho is with the Department of Electrical and Electronic Engineering, the University of Manchester, Manchester, UK. Email: murilo.marinho@manchester.ac.uk. He is also a visiting researcher with the School of Medicine, the University of Tokyo, Tokyo, Japan.

Kanako Harada is with the Schools of Medicine and Engineering, the University of Tokyo, Tokyo, Japan. Email: kanakoharada@g.ecc.u-tokyo.ac.jp.

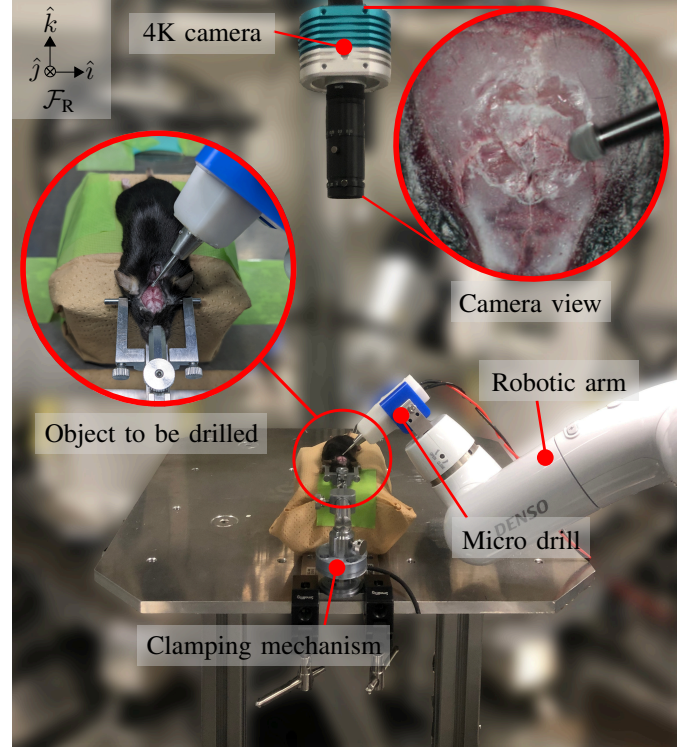


Fig. 1. The system setup used in this work, consisting of one of the 8 degrees-of-freedom robotic branches of our AI-robot platform for scientific exploration [1]. For this work, we attached a micro drill as end effector. In addition, we use a 4K camera and a clamping mechanism for the object being drilled.

Robotic systems have the potential to overcome many of the challenges associated with cranial windowing in mice, by automation of repetitive tasks reducing the task time and enhancing the quality of the experiments. Numerous devices and robotic systems have been devised to aid in cranial window creation. Phuong *et al.* [3] created a robotic stereotaxic platform for small rodents, amalgamating a skull profiling sub-system with a six-degrees-of-freedom robotic platform. Ghanbari *et al.* [4] designed a cranial microsurgery platform, based on a customized computer numerical control mill, for precise microsurgical tasks. Pak *et al.* [5] devised a cranial drilling robot capable of discerning whether the mouse cranium has been penetrated, using conductance measurements for automated craniotomies. Our team is investigating the possibility of autonomously conducting scientific experiments using a robotic manipulator retrofitted with a micro-drill [1], as shown in Fig. 1, with cranial window installation being one of the intended automation targets.

As an end-goal, cranial window procedures must be con-

ducted on anesthetized mice given the nature of the experiments. However, relying on live mice for studying autonomous robot control in relatively early stages of research raises ethical concerns. Therefore, initially we rely on training procedures used for human technical specialists [6] and surgical trainees [7], which comprises in removing a circular patch of chicken eggshell without damaging the underlying membrane.

In our previous research [8], we developed an autonomous robotic drilling system, and we have preliminarily validated its efficacy in autonomously drilling eggshells using image feedback. In this work, we further increased the system efficacy and speed in eggshell drilling by additionally using force information and a plane fitting algorithm. With these sizable improvements, in this work, we show the first-in-the-World example of effective mouse drilling without pre-processing on *postmortem* mice, which is a large step towards the automation of the cranial window procedure in live mice.

#### A. Related works

Developing an autonomous robot drilling system necessitates a thorough understanding of perception. Numerous studies have focused on estimating drilling penetration and status through various signals during human bone drilling procedures. Loschak *et al.* [10] designed a cranial drilling tool with retracting drill bit based on the perception of instantaneous reduction in force upon skull penetration. Hu *et al.* [9] proposed a real-time force-sensing algorithm to discern five key states and determine drill position during spinal orthopedic surgery by analyzing force signals during the screw-path-drilling process. Dai *et al.* [11] successfully estimated screw or drill position relative to the bone and drilling penetration by analyzing electrical impedance signals. Additionally, they proposed a condition monitoring method based on vibration analysis, correlating bone vibration amplitude with its status change during drilling [12]. Ying *et al.* [13] found that measuring force and sound signals during drilling is more effective, achieving high precision estimates of drilling progress with neural networks.

Given the similarities and differences between drilling human bones and mouse craniums, several studies aimed to improve robot perception in mouse cranium drilling surgery. Pohl *et al.* [14] designed a module for assisting mouse craniotomy by measuring force and sound signals, estimating drilling penetration, and controlling drill feed speed. Pak *et al.* [5] demonstrated a penetration detection strategy using a measurement circuit that detects electrical conductance between the drill and the mouse, indicating skull penetration by a sudden increase in conductance. These studies based on the perception of contact signals such as force, sound, and electrical signals are always designed for a single hole drilling on mice skull instead of drilling along a continuous trajectory since the signals for perception are generated solely during the contact, which will result in a lack of global awareness along trajectory.

In order to enhance the drilling system's ability to perceive global information, Ghanbari *et al.* [4] developed a cranial microsurgery platform "Cranibot" that employs a surface

profiler and micro-computed tomography to assess skull surface topology and thickness. These data are utilized to create a 3D milling path towards the desired depth. Jeong *et al.* [15] utilized the metrology via second harmonic generation to map mouse skull surfaces and establish a drilling path, then employed plasma-mediated laser ablation for drilling purposes. Hasegawa *et al.* [16] proposed a drilling system on egg model generating initial drilling trajectory by touching the surface, then drilling downward a certain offset in each loop and judged the local penetration by a integration of force and sound information.

However, obtaining the pre-operative information of the plane to be drilled would take much time before experiment, and some of them introduce advanced sensor with high cost, which make the methods to be impractical to implement broadly. Furthermore, over-reliance on pre-operative information may result in the system's inadequate execution-time feedback on unexpected situations.

In our previous work [8], we developed an autonomous robotic drilling system for mice cranial window creation with only image-based penetration recognition as the perception on global information and preliminarily proved its feasibility by eggshell drilling experiment. However, the lack of local contact information still addresses some limitations in updating lag of recognized penetration of obscured areas by drill and lacking in sufficient accuracy, particularly for pixels with completion levels higher than 0.8. Jia *et al.* [17] presented a 3-phase periodic Bayesian reinforcement learning method for the task of eggshell drilling task as a simulation of cranial window creation, and achieved in successfully drilling and automatically acquiring spatial information about the eggshell terrain via the information of 2D image, force and audio signal instead of 3D scanning in advance. This work combined processing of contact signals and global awareness along trajectory, and does not require any pre-operative information input. Regrettably, the work was evaluated via eggshell model instead of euthanized mice, and the Bayesian reinforcement learning need a dedicated simulator for training, preventing its practicality to implement broadly.

Considering the limitations of previous studies, our aim is to propose an autonomous robotic drilling system for mice cranial window that is able to perceive both contact signals and global information without pre-processing. To achieve this, our system primarily relies on image processing using a neural network for perception, while force signals serve as auxiliary inputs. The contrast of the capabilities of the proposed work with existing literature are shown in Table I.

1) *Image processing*: The neural network utilized for image processing must fulfill two functions: detecting the drilled area and estimating pixel-wise drilling completion levels. Research has shown that these tasks mutually benefit from each other in terms of accuracy during training [18].

In line with these objectives, both fast R-CNN and faster R-CNN [19], [20] can utilize a CNN to extract the bounding box of the target, which is subsequently refined using non-maximum suppression. Building upon this, mask R-CNN [21] extends faster R-CNN by incorporating a parallel branch for predicting object masks alongside the existing branch

TABLE I  
CAPABILITIES OF THE PROPOSED WORK IN CONTRAST WITH EXISTING LITERATURE.

	This work	[4]	[5]	[8]	[9]	[10]	[11]	[12]	[13]	[14]	[15]	[16]	[17]
For mice skull drilling	✓	✓	✓	✓	×	×	×	×	×	✓	✓	✓	✓
Drilling Automation	✓	✓	✓	✓	×	✓	×	×	×	×	✓	✓	✓
Validated on euthanized mice	✓	✓	✓	×	×	×	×	×	×	✓	✓	×	×
Contact signals	✓	✓	✓	×	✓	✓	✓	✓	✓	✓	✓	✓	✓
Global awareness along trajectory	✓	✓	✓	✓	×	×	×	×	×	×	✓	×	✓
Execution-time feedback	✓	×	×	✓	✓	✓	✓	✓	✓	✓	✓	✓	✓
No pre-operative information	✓	×	×	✓	✓	✓	✓	✓	✓	✓	×	×	✓
Practical to implement broadly	✓	×	×	✓	✓	×	×	✓	✓	✓	×	✓	×

for bounding box recognition. While providing high accuracy, it comes with a comparatively slower inference speed. Additionally, the widely-used object detector Single Shot Detector (SSD) [22] directly classifies all boxes through a sliding window technique. To detect objects of varying sizes in a single forward pass, SSD constructs a scale pyramid. Deconvolutional Single Shot Detector (DSSD) [23] is a network built upon SSD’s foundation, merging a state-of-the-art classifier (ResNet-101) with a rapid detection framework (SSD). It further enhances object detection and recognition by introducing deconvolution layers to SSD+ResNet-101, thereby incorporating additional large-scale context.

Given DSSD’s architecture with deconvolutional layers, it is natural to explore semantic segmentation within the same network, as the purpose of these layers is to increase the resolution of output feature maps. Other network architectures [18], [24]–[26] also aim to perform semantic segmentation and object detection simultaneously, inspired by this characteristic. Our work is influenced by these previous attempts, with semantic segmentation replaced by completion level recognition.

2) *Force data processing*: As for the processing of force data, given the time-consuming nature of the mice cranial creation procedure and the potential relevance of drilling completion status to both the current and previous system states, Recurrent Neural Networks (RNNs) emerge as promising options. RNNs can not only learn existing features but also incorporate previous information, setting them apart from traditional neural networks and making them widely employed in time series applications [27]. However, RNNs suffer from the problem of gradient explosion [28]. To overcome this limitation and effectively process long-term sequences, Long-Short Term Memory (LSTM) units have been introduced, exhibiting strong performance [29]. The LSTM-RNN has demonstrated notable success in diverse applications, including clinical diagnosis [30], image segmentation [31], and language modeling [32]. Furthermore, LSTM-RNN is proved to not only deal with the drift and noise in the signal but also do real-time signal processing compared with other signal processing methods for the force sensor signal processing [33]. And He *et al.* [34] showed that LSTM-RNN can be applied to oversee surgeon’s operation and predict possible unsafe scleral forces up to the next 200 milliseconds relying on the force data collected over the past period of time in retinal microsurgery. Consequently, it is a natural choice to contemplate using LSTM-RNN for our system to process the force sensor signal in real-time.

## B. Statement of contributions

In this work, we build upon previous [8] with an improved trajectory planner and a multimodal recognition system with image and force information, enabling the operation in *post-mortem* mice. In detail, we propose (1) a trajectory planning algorithm based on constrained splines and execution-time plane fitting that is adjusted in real time by image, and force feedback, (2) a drilling completion level recognition module based on deep neural networks with multi-branch architectures to update the planner trajectory at execution-time with image and force information. The force information increases completion-level recognition resolution 10 times. In addition, we (3) evaluate our method in robotic drilling experiments using eggshells and provide the World’s-first results in cranial window drilling in *postmortem* mice.

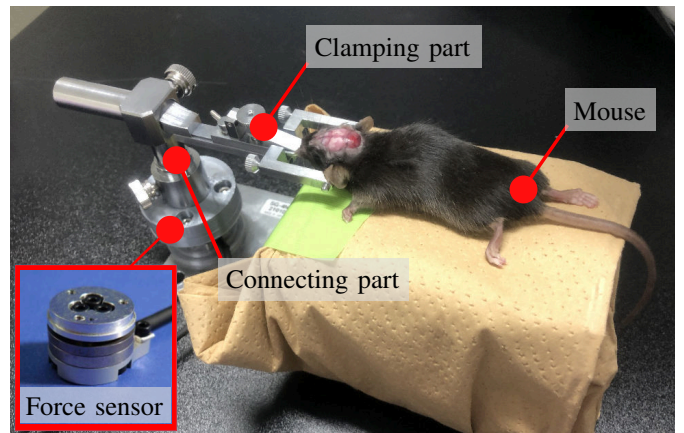


Fig. 2. The clamping mechanism for mouse skulls including a commercial mouse skull holder and a force sensor.

## II. PROBLEM STATEMENT

Consider the setup shown in Fig. 1, using one of the robotic arms of our robot platform for scientific exploration [1]. Let  $R$  be the 8-degrees-of-freedom serial manipulator with joint values  $\mathbf{q} \in \mathbb{R}^8$  composed of the robotic arm (CVR038, Densowave, Japan), linear actuator, and circular rail actuator. Let  $R$  be holding the micro drill (MD1200, Braintree Scientific, USA). The micro drill is used to drill the object (i.e. either the eggshell or the mouse skull) that is fixed by our clamping platform. The clamping platform contains a force sensor (ThinNANO, BL AUTOTEC, Japan). For mice, the clamping part is a head holder (SG-4N, NARISHIGE, Japan),



shown in Fig. 2. And for eggs it is a custom-designed 3D printed egg holder. The force sensor has a custom-designed 3D printed casing to fix the force sensor underneath the egg holder, shown in Fig. 3. Images are obtained from above through a 4K microscope system (STC-HD853HDMI, Omron-Sentech, Japan) equipped with a distortionless macro lens of  $f = 75$  mm (VS-LDA75, VS Technology, Japan).

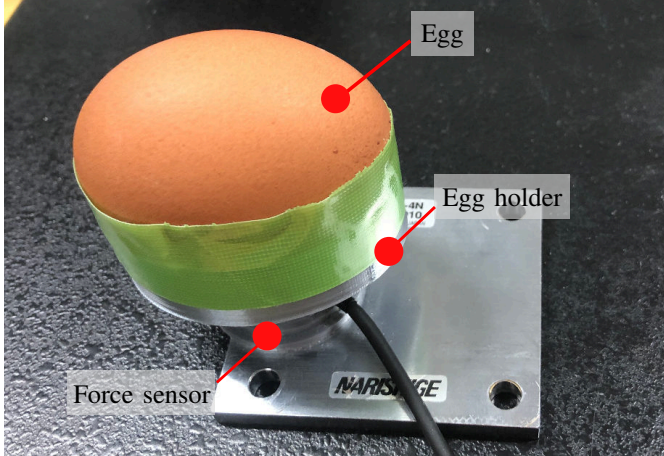


Fig. 3. The clamping mechanism for eggs including a 3D printed holder and a force sensor.

#### A. Goal

Our goal is to autonomously drill the object (eggshell or mouse skull) along a circular path with respect to the base frame of the robot system,  $\mathcal{F}_R$  (see Fig. 1), for suitable objects without target-specific data collection, pre-processing, or surface measuring stage. In addition to proprioceptive information (kinematics and encoders), the goal is to use image and force as feedback during execution time.

### III. PROPOSED AUTONOMOUS DRILLING METHOD BASED ON MULTI-SENSOR FUSION

The overview of the proposed method is shown in Fig. 4. In our strategy, the drill is autonomously along a trajectory (introduced in Section III-A) in the  $x$ - $y$  plane while the  $z$ -axis coordinate of each point is updated by the completion level recognition (introduced in Section III-B).

#### A. Trajectory planning

The exteroceptive completion level recognition module outputs a discrete set of  $n$  points ( $n = 32$  for [8] using only image and  $n = 320$  for the proposed image and force module). Nonetheless, the robot must be given a continuous trajectory for smooth performance using our inverse kinematics calculation [1].

In formal terms, let the desired drill path be discretized into  $n$  equal intervals resulting in the points  $\mathbf{p}_i(c_i) \triangleq [p_{x,i} \ p_{y,i} \ p_{z,i}(c_i)]^T \in \mathbb{R}^3$ ,  $i = 1, \dots, n \in \mathbb{N}$ , defined with respect to the base frame of the robotic manipulator  $\mathcal{F}_R$  (see Fig. 1). In addition, let  $c_i \triangleq c_i(t)$  be the completion level of each point  $i$  obtained by the camera and/or force

sensor, where  $c_i = 0$  means not drilled and  $c_i = 1$  means completely drilled. The goal of the trajectory planner is to obtain a continuous trajectory that is circular *when projected* in the  $x$ - $y$  plane and causes all  $n$  drill points to be complete in finite time by updating the  $z$ -axis position,  $p_{z,i}$ , using the completion level  $c_i$ . We hypothesize that, by using a proper interpolation methodology, if all  $n$  points (the ones we can effectively measure online) are sufficiently drilled, then the entire trajectory (including the points that we cannot directly measure) will be sufficiently drilled.

The proposed trajectory planner is divided into three steps. First, imbued with each completion level (obtained Section III-B),  $c_i$ , we calculate each  $p_{z,i}(c_i)$  as shown in Section III-A1. Second, a plane is fitted based on those points  $\mathbf{p}_i(c_i)$  whose completion level  $c_i \neq 0$ , obtaining an offset  $o_{z,i}$  between each point and its projection on the plane to update  $p_{z,i}(c_i)$  on the trajectory as shown in Section III-A3. Lastly, with the  $z$ -axis coordinate for each of the  $n$  measure points defined in the previous step, we use the desired trajectory topology to obtain the continuous drill path using a constrained spline interpolator as shown in Section III-A2.

1)  *$z$ -axis trajectory calculation: multimodal velocity damper*: The core of our automatic drilling proposal is to reduce the downward velocity  $v_{z,i} \triangleq v_{z,i}(c_i) \in \mathbb{R}$  of a given trajectory point  $i$  proportionally to its level of completion  $0 \leq c_i \leq 1$ , obtained via multimodal information as shown in Section III-B. The velocity is modulated as follows

$$v_{z,i}(c_i) = (1 - c_i) v_z. \quad (1)$$

This means that when a trajectory point  $i$  has completion level  $c_i = 0$ , it is untouched, hence  $v_{z,i}(0) = v_z$  and the robot moves at nominal velocity  $v_z$  downward, where  $v_z$  is a design parameter with a negative value (e.g. -1 mm/s), since the upward direction is defined as the positive direction in the base frame of the robot system  $\mathcal{F}_R$ . When the trajectory point has  $c_i = 1$ , that point has been fully drilled and the downward velocity becomes  $v_{z,i}(1) = 0$ , meaning that the robot will not drill further. Intermediate levels of completion allow the system to behave smoothly with respect to the level of completion.

Although effective, a direct implementation of (1) has been shown in our previous work [8] not time-efficient when the target circular drill surface is not aligned with the robot's  $x$ - $y$  plane.

In this work, we augment (1) with an online estimation of the target  $x$ - $y$  drill plane using  $c_i$ , described in detail in Section III-A3. Considering the simple integration of (1) with a sampling time  $T$ , the plane-fitted position-based algorithm becomes

$$p_{z,i}(t + T) = p_{z,i}(t) + v_{z,i}(c_i)T + o_{z,i}(t), \quad (2)$$

where  $o_{z,i}(t)$  is the plane-fitted offset, detailed in Section III-A3. This way, the drilling traverses through empty space much faster by estimating the surface plane of the target and adapting accordingly.

2) *Continuous trajectory generation: constrained cubic spline interpolation*: Since the  $z$ -axis coordinate for each of the  $n$  measure discrete points  $p_{z,i}(c_i)$  has been updated in the



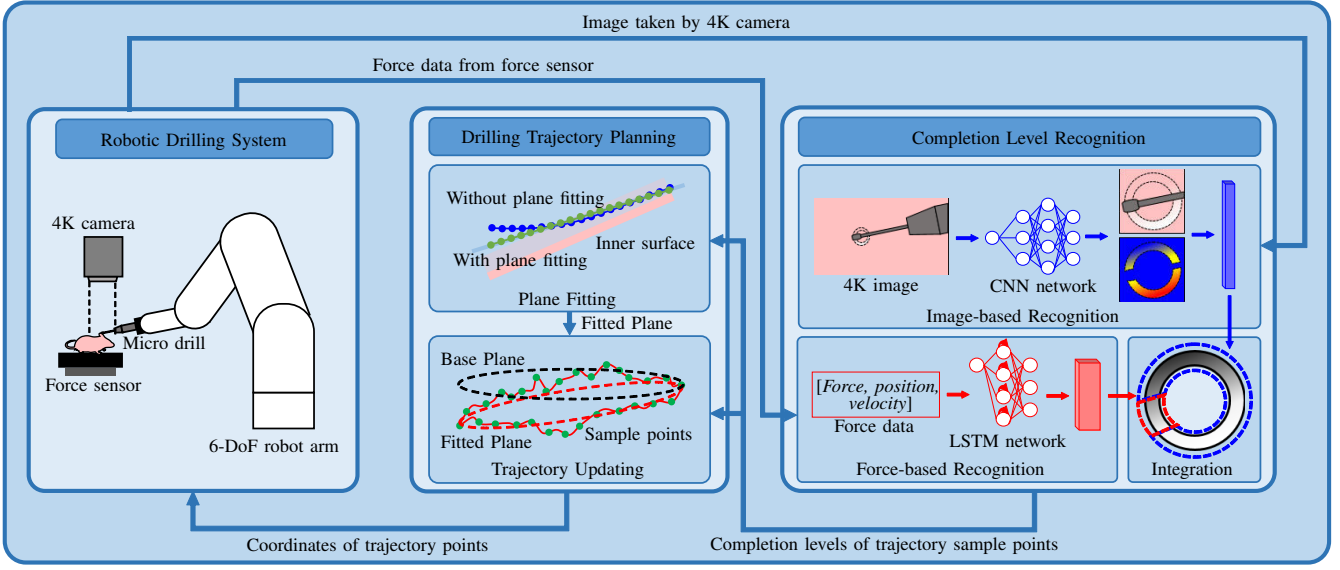


Fig. 4. Block diagram of the autonomous robotic drilling system. The robotic system block interacts with the object to be drilled (eggshell or mouse skull). A 4K camera provides images and a force sensor provides force information to the completion level recognition block. The completion level recognition block integrates the estimation result based on image and force information and outputs the completion levels of trajectory measure points for the trajectory planning block. Based on the completion level, the trajectory planning block updates the continuous trajectory at execution time. The trajectory is processed by the constrained inverse kinematics algorithm [1], which outputs joint commands to the robotic system, closing the loop.

previous section, the purpose of this section is to generate a continuous drilling path based on these points to match the high precision encoders used in the robotic system. Cubic spline interpolation has been widely applied for generating continuous path from discrete points but it is, by itself, unsuitable for our application as it might overshoot between two trajectory measure points and cause rupture to the membrane (see Fig. 5). Instead, we propose the use of constrained spline interpolation by eliminating the requirement for equal second order derivatives at every point and replacing it with specified first order derivatives [35]. As an improvement over our previous work [8], we focus on the relevant coordinates given that our trajectory is cylindrical.

Let the trajectory points be  $[p_{x,i} \ p_{y,i} \ p_{z,i}]^T$ ,  $i = 1, \dots, n \in \mathbb{N}$ . We express them under a cylindrical coordinate system  $[p_{\rho,i} \ p_{\varphi,i} \ p_{z,i}]^T$ . The  $z$ -axis coordinate  $p_{z,i}$  is the same for both expressions while

$$p_{\rho,i} \triangleq \sqrt{p_{x,i}^2 + p_{y,i}^2} = r,$$

$$p_{\varphi,i} = \arctan\left(\frac{p_{y,i}}{p_{x,i}}\right),$$

where  $r$  is the radius of the cylinder, which is a constant value of 4 mm in our setup. As a result, interpolation happens in  $\mathbb{R}^2$ , namely the points  $\boldsymbol{\rho}_i = [p_{\varphi,i} \ p_{z,i}]^T$  with  $p_{\varphi,i} \in [0, 2\pi) \subset \mathbb{R}$  and  $p_{z,i} \in \mathbb{R}$ .

Let  $\varphi$  be the independent variable to generate a curve  $\boldsymbol{s}(\varphi) = [\varphi \ s_z(\varphi)]^T$  through  $[0, 2\pi)$ . We have then a set of piecewise curves  $\boldsymbol{s}_i(\varphi) = [\varphi \ s_{z,i}(\varphi)]^T$ , each  $i$ -th curve describing a curve between two contiguous points  $\boldsymbol{\rho}_i$  and  $\boldsymbol{\rho}_{i+1}$ . By the definition of a cubic spline, each curve is a third-degree polynomial given by

$$s_{z,i}(\varphi) \triangleq a_{z,i} + b_{z,i}\varphi + c_{z,i}\varphi^2 + d_{z,i}\varphi^3, \quad (3)$$

whose first-order derivative of (3) is

$$\dot{s}_{z,i}(\varphi) \triangleq b_{z,i} + 2c_{z,i}\varphi + 3d_{z,i}\varphi^2. \quad (4)$$

In order to calculate the parameters of the curve, we need three continuity conditions. First, given that the domain for each  $\boldsymbol{s}_i(\varphi)$  is  $[p_{\varphi,i}, p_{\varphi,i+1}]$ , each piecewise curve must pass through its “left” endpoint  $\boldsymbol{p}_i$  and “right” endpoint  $\boldsymbol{p}_{i+1} = [p_{\varphi,i+1} \ p_{z,i+1}]^T$ , that is,

$$s_{z,i}(p_{\varphi,i}) \triangleq p_{z,i}, \quad (5)$$

$$s_{z,i}(p_{\varphi,i+1}) \triangleq p_{z,i+1}. \quad (6)$$

Second, the first-order derivative of the whole curve must be continuous, which means the whole curve is continuously differentiable at each  $\boldsymbol{p}_i$ . Its first-order derivative,  $\dot{p}_{z,i}$ , is a free parameter. In traditional cubic spline interpolation, the third condition is to define the second-order derivative for each measure point as  $\ddot{p}_{z,i}$ . As a result, the generated trajectory is smooth enough but overshoot might occur.

For constrained cubic spline interpolation, instead, we aim to solve the overshoot problem by sacrificing smoothness. We constrain the first-order derivative to prevent overshoot between two contiguous points as

$$\dot{s}_{z,i}(p_{\varphi,i}) \triangleq \dot{p}_{z,i}, \quad (7)$$

$$\dot{s}_{z,i}(p_{\varphi,i+1}) \triangleq \dot{p}_{z,i+1}, \quad (8)$$

where the intention is to ensure that the first order derivative at a point will be between the slope of the two adjacent lines joining that point, and should approach zero if the slope of either line approaches zero. Furthermore, the first order derivative of a point should be 0 if the signs of the slope of the two lines are different from each other to define this point as a local minimum to prevent overshoot. To define a

first order derivative that satisfies the conditions, we denote the product of the differences between the  $z$ -coordinates of a point  $p_{z,i}$  and its left point  $p_{z,i-1}$  and right points  $p_{z,i+1}$  as

$$t_i \triangleq (p_{z,i+1} - p_{z,i})(p_{z,i} - p_{z,i-1}), \quad (9)$$

so the first order derivative at the point can be calculated as

$$\dot{p}_{z,i} \triangleq \begin{cases} \frac{2}{\frac{p_{\varphi,i+1}-p_{\varphi,i}}{p_{z,i+1}-p_{z,i}} + \frac{p_{\varphi,i}-p_{\varphi,i-1}}{p_{z,i}-p_{z,i-1}}} & \text{if } t_i > 0 \\ 0 & \text{otherwise} \end{cases}. \quad (10)$$

It is important to note that (9) and (10) are only valid when  $2 \leq i \leq n-1$ . Considering the projection of the curve on the  $x$ - $y$  plane is a circle, the first point and the end point of the trajectory are adjacent. We can define  $t_1 \triangleq (p_{z,2} - p_{z,1})(p_{z,1} - p_{z,n})$  and  $t_n \triangleq (p_{z,1} - p_{z,n})(p_{z,n} - p_{z,n-1})$ . So when  $t_1 > 0$  or  $t_n > 0$ , (10) can be adjusted to obtain

$$\dot{s}_z(p_{\varphi,1}) = \dot{p}_{z,1} \triangleq \frac{2}{\frac{p_{\varphi,2}-p_{\varphi,1}}{p_{z,2}-p_{z,1}} + \frac{p_{\varphi,1}-(p_{\varphi,n}-2\pi)}{p_{z,1}-p_{z,n}}}, \quad (11)$$

$$\dot{s}_z(p_{\varphi,n}) = \dot{p}_{z,n} \triangleq \frac{2}{\frac{(p_{\varphi,1}+2\pi)-p_{\varphi,n}}{p_{z,1}-p_{z,n}} + \frac{p_{\varphi,n}-p_{\varphi,n-1}}{p_{z,n}-p_{z,n-1}}}. \quad (12)$$

We can calculate all coefficients by combining (3), (4), (5), (6), (7), and (8) into

$$\begin{bmatrix} a_{z,i} \\ b_{z,i} \\ c_{z,i} \\ d_{z,i} \end{bmatrix} = \begin{bmatrix} 1 & p_{\varphi,i} & p_{\varphi,i}^2 & p_{\varphi,i}^3 \\ 1 & p_{\varphi,i+1} & p_{\varphi,i+1}^2 & p_{\varphi,i+1}^3 \\ 0 & 1 & 2p_{\varphi,i} & 3p_{\varphi,i}^2 \\ 0 & 1 & 2p_{\varphi,i+1} & 3p_{\varphi,i+1}^2 \end{bmatrix}^{-1} \begin{bmatrix} p_{z,i} \\ p_{z,i+1} \\ \dot{p}_{z,i} \\ \dot{p}_{z,i+1} \end{bmatrix} \quad (13)$$

By substituting (10), (11), and (12) into the right side of (13), we can get the value of coefficients expression  $a_{z,i}$ ,  $b_{z,i}$ ,  $c_{z,i}$ , and  $d_{z,i}$ . We can obtain the expression of any piecewise third-degree polynomial curves  $s_i(\varphi)$  and, consequently, know the entire curve  $s(\varphi)$ . The cylindrical coordinates are mapped back into the Cartesian space  $\mathcal{F}_R$  before going into the manipulator's inverse kinematics calculation [1]. Figure 5 shows a qualitative comparison between a traditional cubic spline interpolation and its constrained version. This is to show that the green curve is enveloped by the tangent planes but red curve is not, hence illustrating the problem of overshoot.

3) *Plane fitting*: As mentioned in our former study [8], the problem of the long drilling time and high failure rate is mostly caused by a tilted initial pose. In this work we address this issue with an execution-time plane fitting.

To achieve this, we first divide the drilling procedure into three steps: before touching the eggshell, touching the eggshell at part of the points, and touching the eggshell at all points. Steps can be differentiated by the completion level of trajectory points that is calculated in Section III-B. At the step of before touching the eggshell, the completion level of all trajectory points are supposed to be 0. At the step of touching the eggshell at part of the points, the completion level of the trajectory points that have still not touched the eggshell yet remain 0 but those that have touched the eggshell change to values larger than 0. And finally, if the completion level of all the trajectory points become larger than 0, the step goes to touching the eggshell at all points.

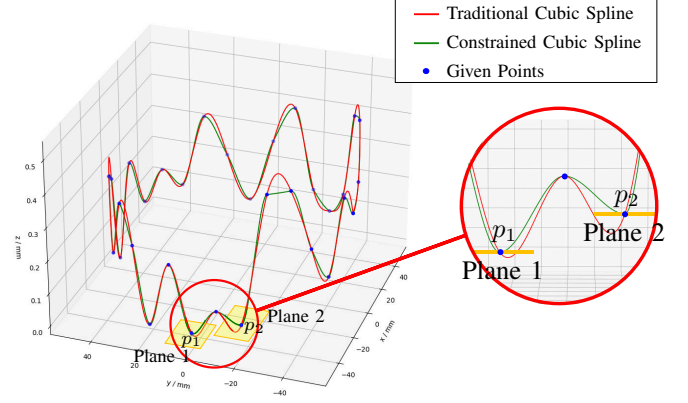


Fig. 5. Generated curve based on a certain amount of measure points along the circular path. The blue points are the measure points, the red line is the result of traditional spline interpolation, and the green line is the result of constrained spline interpolation. We can see the red line overshoots while the green does not.

During the step of touching the eggshell at part of the points, the tilted initial pose of egg may result in long drilling time and high failure rate by causing drill to touch the eggshell at one point on the drilling trajectory sooner than another, while the other two steps will not be influenced. As a result, we are trying to apply a plane fitting method to accelerate the drilling procedure during the step of touching the eggshell at part of the points.

Let there be  $n \in \mathbb{N}$  points be described in Cartesian coordinates  $\mathbf{r}_i \triangleq [p_{x,i} \ p_{y,i} \ p_{z,i}]^T$ , for which we want to fit a plane. We start with the general equation of a plane

$$a_x x + a_y y + a_z z + a = 0 \quad (a_z \neq 0).$$

Collapsing this into an expression for the  $z$ -coordinate

$$z = a_0 x + a_1 y + a_2, \quad (14)$$

where

$$a_0 = -\frac{a_x}{a_z}, \quad a_1 = -\frac{a_y}{a_z}, \quad a_2 = -\frac{a}{a_z}.$$

Applying least squares method, we try to minimize the sum of square of distance between each trajectory point and its projection on the plane as

$$S = \sum_{i=1}^n (a_0 p_{x,i} + a_1 p_{y,i} + a_2 - p_{z,i})^2.$$

To minimize  $S$ , we need the partial derivative of  $S$  with respect to  $p_{x,i}$ ,  $p_{y,i}$  and  $p_{z,i}$  and make them to be 0, that is

$$\begin{cases} \frac{\partial S}{\partial a_0} = 2 \sum_{i=1}^n (a_0 p_{x,i} + a_1 p_{y,i} + a_2 - p_{z,i}) p_{x,i} = 0 \\ \frac{\partial S}{\partial a_1} = 2 \sum_{i=1}^n (a_0 p_{x,i} + a_1 p_{y,i} + a_2 - p_{z,i}) p_{y,i} = 0 \\ \frac{\partial S}{\partial a_2} = 2 \sum_{i=1}^n (a_0 p_{x,i} + a_1 p_{y,i} + a_2 - p_{z,i}) = 0 \end{cases}.$$

Solve the system of equations, we can get

$$\begin{bmatrix} a_0 \\ a_1 \\ a_2 \end{bmatrix} = \mathbf{A}^{-1} \mathbf{b}, \quad (15)$$

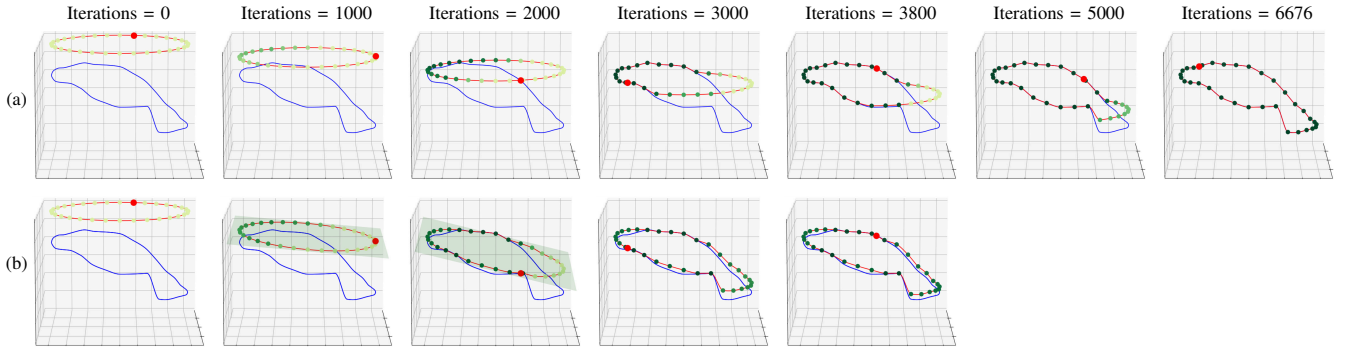


Fig. 6. Two series of snapshots of the updated trajectory using trajectory planner (a) without plane fitting based on real robot experiment data (described in Section III-A2) while (b) with plane fitting in simulation (described in Section III-A3). The blue line is the target curve to which both trajectory planners are adapted. The red line is trajectory that is updated in real time. The color of the points in the trajectory change based on their completion level. The red point refers to the current position of the drill.

where

$$\mathbf{A} = \begin{bmatrix} \sum_{i=1}^n p_{x,i}^2 & \sum_{i=1}^n p_{x,i}p_{y,i} & \sum_{i=1}^n p_{x,i} \\ \sum_{i=1}^n p_{x,i}p_{y,i} & \sum_{i=1}^n p_{y,i}^2 & \sum_{i=1}^n p_{y,i} \\ \sum_{i=1}^n p_{x,i} & \sum_{i=1}^n p_{y,i} & n \end{bmatrix}$$

$$\mathbf{b} = \begin{bmatrix} \sum_{i=1}^n p_{x,i}p_{z,i} \\ \sum_{i=1}^n p_{y,i}p_{z,i} \\ \sum_{i=1}^n p_{z,i} \end{bmatrix}$$

So we can get the equation of the fitted plane by solving (15) and substituting the values of  $a_0$ ,  $a_1$  and  $a_2$  into (14).

In our application, instead of using all in the trajectory points, we consider to only use the points whose completion level are not 0 to fit the plane, given that they are the only points about which we have enough information.

After the plane fitting, original points on the trajectory should be updated to the fitted plane. At time  $t$ , consider a certain point on the trajectory  $\mathbf{p}_i(t) \triangleq [p_{x,i}(t) \ p_{y,i}(t) \ p_{z,i}(t)]^T$ , the  $z$  coordinate of the corresponding point on the fitted plane will be

$$p'_{z,i}(t) = a_0 p_{x,i}(t) + a_1 p_{y,i}(t) + a_2.$$

As a result, the offset  $o_{z,i}(t)$  in (2) can calculate by

$$o_{z,i}(t) = p'_{z,i}(t) - p_{z,i}(t).$$

We compared the plane fitting on part of the trajectory points with the plane fitting on all of the trajectory points using both simulation and real eggshell drilling experiment, and proved that the method on part of the points lead to a shorter time for the trajectory adapting to the curve of eggshell, and a negligible overshoot that is expected to have little influence on the success rate of drilling<sup>1</sup>. Furthermore, we tested the trajectory planner with plane fitting on part of the trajectory points in simulation. The surface to be adapted to is set to be the data that we collected with real robot using the trajectory planner without plane fitting (shown in Fig. 6-(a)), discussed in Section III-A2. Iterations are recorded for comparing the drilling time with and without the plane fitting block. A series of snapshots of updated trajectory is shown in Fig. 6-(b). From the image we can see that the trajectory

adapted to the surface faster with plane fitting block, which is in line with our expectation. However, it is important to notice that the final trajectory planned with and without plane fitting can be different even though the target surfaces are the same, considering the error of completion level recognition.

### B. Completion level recognition

The completion level recognition block consists of three parts. Namely, image-based completion level recognition (Section III-B1), force-based completion level recognition (Section III-B2) and completion level results integration (Section III-B3). The image-based and force-based completion level recognition part can independently estimate the drill completion levels for selected measure points on the trajectory, and the two results are integrated for improved performance.

1) *Image-based completion level recognition*: For image-based completion level recognition, we aim to detect the drilling area and estimate the drilling completion level simultaneously using a single neural network. This is because it is known that detection and semantic segmentation benefit from each other in training. The algorithm and network remain unchanged from our previous paper [8], whose architecture is inspired by DSSD [23] and contains two branches for bounding-box detection and completion level recognition<sup>2</sup>. The main difference is that in this paper, a mouse skull dataset is built and applied to retrain the network in preparation for mouse skull drilling experiments.

a) *Training dataset creation*: In our former study [8], we collected 518 images from manual eggshell drilling experiments that comprised the eggshell dataset. In order to apply the system to the mouse skull drilling experiment, 587 images from manual eggshell drilling experiments were collected for mouse skull dataset considering the individual diversity of mouse skulls.

*Data annotation*: Generally, ground truth images with full manual annotation are required for multi-task learning. In this work, we expect our network to output a bounding box of the drilling area and a completion level map. When generating the ground truth of completion level maps, manually annotating

<sup>1</sup>More information available in the supplementary material.

<sup>2</sup>More information available in the supplementary material.



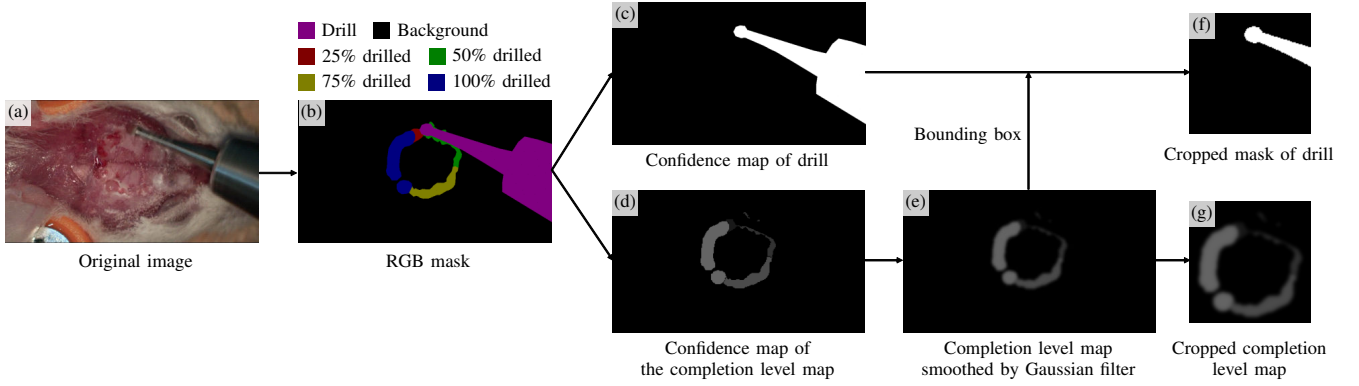


Fig. 7. An example of creating a training dataset. (a) An original image of mouse skull drilling. (b) RGB mask that is labeled manually in 6 classes: Drill, 0% drilled (Background), 25% drilled, 50% drilled, 75% drilled, and 100% drilled. (c) Confidence map of the drill. (d) Confidence map of the completion level map. (e) The completion level map smoothed by a Gaussian filter. (f) Cropped drill mask within the drilling region. (g) Cropped completion level map within the drilling region.

each pixel with a grayscale value ranging from 0 to 100 is not feasible (0 of grayscale refers to the completion level of that pixel  $c = 0$  while 100 refers to  $c = 1$ ). We propose a more treatable annotation strategy.

To describe the annotation procedure, let us use a mouse skull drilling image, but the process is the same for eggshell images. As shown in Fig. 7-(a), given an image, first we define 6 classes for a semantic segmentation classifier: drill, 0% drilled (background), 25% drilled, 50% drilled, 75% drilled, and 100% drilled as shown in Fig. 7-(b). The percentage of drilling completion is defined subjectively with our experience in pilot studies. Second, in a higher level in the hierarchy, we separate the image into confidence maps. The first image is the confidence map for pixels of the drill, as shown in Fig. 7-(c), with 255 corresponding to the full confidence, so that the drill can be removed from the image. The second confidence map corresponds to the completion level map, as shown in Fig. 7-(d), where 0 of grayscale corresponds to 0% drilled pixels and 100 corresponds to 100% drilled pixels. Lastly, taking advantage of the expected continuity in drilled regions, a Gaussian filter is applied to smooth the completion level map channel so that its grayscale values of pixels are continuous from 0 to 100, as shown in Fig. 7-(e).

The bounding box is automatically annotated. A 4-dimensional vector  $(x_1, y_1, x_2, y_2)$  is used as the ground truth of the bounding box detection branch, which is generated from the completion level map channel by noting the minimum value and maximum value from width and height direction of those pixels whose grayscale values are not 0. After that, we crop both the completion level map channel and drill channel using the coordinate of the bounding box  $(x_1, y_1)$  and  $(x_2, y_2)$  and then resize them into  $128 \times 128$ . Merging two channels together we can get a  $128 \times 128 \times 2$  matrix as the ground truth of the completion prediction branch, as shown in Fig. 7-(f)(g).

*Dataset augmentation:* At the training stage, we used common image augmentation methods: random flip, rotate, random crop, and random change of brightness and contrast.

We manually labeled 518 eggshell images and 16,576 after augmentation for eggshell dataset, and 587 mouse skull images and 18,784 after augmentation for mouse skull dataset. 80%

of those images were used for training, 10% were used for validation and 10% were used for testing. More details on the training are available in the supplementary material.

*b) Loss function:* The loss function of our training procedure contains three parts: the loss function of bounding box detection  $L_{bb}$  for the drilling area, the loss function of the drill semantic segmentation  $L_{drill}$  for the drill, and the loss function of the completion prediction  $L_{com}$ .

We obtain  $L_{bb}$  as a weighted sum of the localization loss  $L_{loc}$  and the confidence loss  $L_{conf}$ , given by

$$L_{bb} = \frac{1}{N} (L_{loc} + L_{conf}). \quad (16)$$

where  $N$  is the number of matched default boxes. If the number of matched default boxes is 0, we set  $N$  as 1.

We obtain  $L_{drill}$  as a weighted sum of dice loss  $L_{dice}$  and boundary loss  $L_b$ , given by

$$L_{drill} = \alpha L_{dice} + (1 - \alpha) L_b. \quad (17)$$

where  $\alpha = \max(0.01, 1 - 0.01 \times epoch)$ . We can see that as the training process progresses, the weight of  $L_b$  continuously increases.

Lastly,  $L_{com}$  is L2 loss function which calculates the addition of the absolute value of the difference of each according pixel.

The overall loss function  $L$  is given by

$$L = L_{bb} + L_{drill} + L_{com}. \quad (18)$$

In pilot experiments we could not observe significant improvements in results for different weights in the loss functions.

*c) Transfer learning:* In our former study [8], a network was trained using eggshell dataset. Considering the similarity between eggshell and mouse skull drilling images, we apply the approach of transfer learning and regard the eggshell model as the pre-trained model and use as starting point for the mouse skull dataset.

*d) Training result and evaluation:* The output results of an eggshell image and an mouse skull image are shown in Fig. 8. The network is able to output a bounding box for drilling area and the cropped image of the area. The

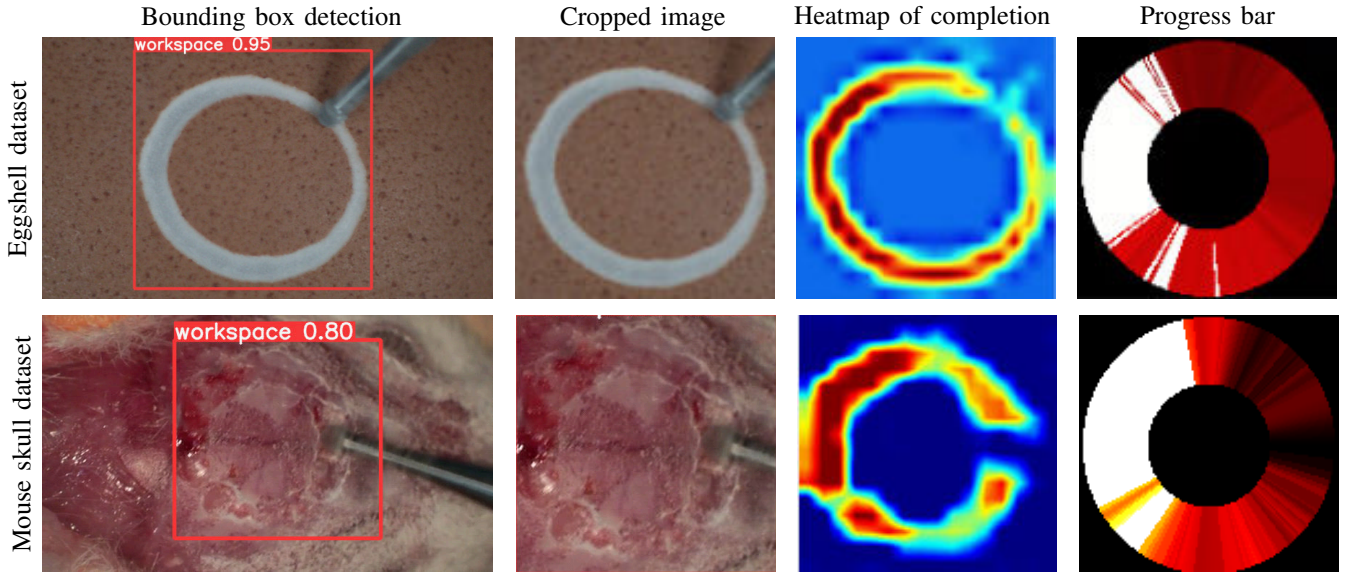


Fig. 8. Output result from the network. The original image with bounding box, the cropped image, heatmap and progress bar of completion level map are output for post processing and visualization.

completion levels of parts that are drilled and not occluded by the drill are shown in the completion level map, while untouched or occluded parts are suppressed.

mAP (mean Average Precision) is applied as the evaluation metric for the object detection while MAPE (Mean Absolute Percentage Error) is applied as the evaluation metric of completion prediction task. Our network architecture is able to reach up 78.5 in mAP for detection and 15.05% in MAPE for prediction while the speed is 72 Hz for the eggshell dataset. For the mouse skull dataset, the speed is unchanged, the mAP for detection is 77.6, and the MAPE for prediction is 24.32%. Reasonable values in this application are  $\text{mAP} > 75$ ,  $\text{MAPE} < 25\%$  and real-time ( $\text{fps} > 60$  Hz), so our work is able to achieve the a good trade-off.

We obtain a progress bar by normalizing the corresponding pixel value. The progress bar is generated by not only the completion level map in this moment but also those in the past because we expect the drilling progress of an area to be monotonically increasing. By setting  $m$  discrete points evenly along the circle on the progress bar, a  $c_{\text{image}}$  with size of  $m$  and elements  $c_i \in [0, 1] \subset \mathbb{R}$ , namely the completion level any points  $i$  and  $i = 1, \dots, m \in \mathbb{N}$ . The value of  $m$  is 32 considering the resolution of the image.

2) *Force-based completion level recognition*: The force based completion level is an addition over [8]. In order to compensate for the inaccuracy of image processing in estimating results when the completion level is higher than 0.8, to address occlusion of points by the drill, and to increase spatial resolution, we added a force-based Long Short-Term Memory Recurrent Neural Network (LSTM-RNN) [29]. This approach takes advantage of the higher spacial accuracy of the force information (w.r.t. image information) and the significant difference in stiffness between the membrane and the skull or eggshell. We utilize force data collected during the surgical procedure to predict the completion level at the current and subsequent drilling regions.

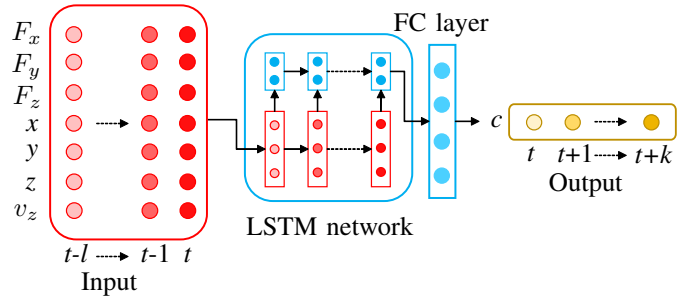


Fig. 9. The LSTM-RNN under consideration receives input from the historical data spanning  $l$  seconds in the past. It then generates recognition results for the completion levels from time  $t$  to  $t+k$ , where  $t$  is the current moment, and  $k$  is the predictable time in the future for the network.

a) *Network architecture*<sup>3</sup>: We posit that predicting the completion levels in the vicinity of the drill-surface contact area can be achieved by analyzing the measurement values of force sensor and the position and velocity state of the drill over a short history (e.g., the past few seconds). To implement this recognition, we employ an LSTM-RNN whose structure is inspired by [36], as shown in Fig. 9.

b) *Training dataset*: The proposed LSTM-RNN takes the force, the positions, and velocities of the drill in past  $l$  seconds as the input, and outputs the completion levels from time  $t$  to  $t+k$  in the future as the drill moves a complete circular trajectory on the  $x$ - $y$  plane. Note that  $t$  denotes the current moment,  $k$  is the predictable number of future time. Considering our drilling speed of 16 second per turn, we chose the hyper parameters  $l = 16$  and  $k = 4$  considering the size of obscured area. The sampling frequency of the force sensor was set as 20 Hz to obtain input data  $L = 20l$  and output data  $K = 20k$ .

In order to obtain the training dataset, 10 trials of au-

<sup>3</sup>More information available in the supplementary material.

onomous drilling experiment on eggshells and 10 trials of experiments on mice were conducted with only the image processing module described in [8]. Force data in the three coordinates  $F_x$ ,  $F_y$ , and  $F_z$ , position data of the drill  $x$ ,  $y$ , and  $z$ , and the descent speed  $v_z$  at each sampling timestep were recorded. The groundtruth of the completion level  $c$  at the drilling area was annotated manually based on the 4K image taken from above with the same method described in Section III-B1. The force information spatial resolution allows us to have 320 points for the completion level recognition. We adjust the 32 points ground truth obtained by the image and replicate each point 10 fold to have the same amount of points and align the two data out-streams. Denoting that the length of data (drilling time  $\times$  frequency) of one trial as  $S$ , we can get matrix of size  $8 \times S$  with the row  $[F_x \ F_y \ F_z \ x \ y \ z \ v_c \ c]$ . Because the desired input has size  $7 \times L$  and the output has size  $1 \times K$ , we can cut the  $8 \times S$  matrix into  $S-L-K$  sets for training evaluation data from one trial of drilling experiment.

The raw data for eggshell drilling dataset consists 84,000 sample timesteps in total, cut into 80,000 sets of data. The mouse drilling dataset consists 83,600 sets cut from 87,600 sample timesteps. 80% of those sets were used for training, 10% were used for validation, and 10% were used for testing. More details on the training are available in the supplementary material.

*c) Loss function:* The loss function chosen for our task is L2 function because it is the difference between two vectors.

*d) Training result and evaluation:* The LSTM-RNN is expected to output the prediction result of completion level from time  $t$  to  $t+k$  based on the input data from time  $t-l$  to  $t$ . What can be expected is that prediction result of the completion level at time  $t+\Delta t$  ( $0 \leq \Delta t \leq k$ ) should be an implicit variable in  $\Delta t$ . By comparing the prediction result at time  $t+\Delta t$  with the ground truth, the prediction accuracy of the network for  $\Delta t$  time forward can be calculated, denoted as  $acc(\Delta t)$ . In our case we allow a difference between predicted and true value within 0.05.

The curves of changes in accuracy  $acc(\Delta t)$  for the eggshell dataset and the mouse dataset are shown as the red and blue lines in Fig. 10-(a). When  $\Delta t = 0$ , the accuracies of both curves reach their maximum value, 88.60% for eggshell dataset and 77.43% for mouse dataset. As  $\Delta t$  increases, both curves show a decreasing trend. For the eggshell dataset, the lowest accuracy 52.61% occurs when  $\Delta t = 69$ , while for the mouse dataset the lowest accuracy 41.21% is at  $\Delta t = 70$ . The result is in line with our predictions because larger  $\Delta t$  is farther into the future, which is more difficult for the neural network to predict. By linear fitting of the accuracy using the least squares method, we can obtain an expression for the accuracy

$$acc(\Delta t) = a \cdot \Delta t + b (\%). \quad (19)$$

For the eggshell dataset, the values of parameters  $a$  and  $b$  are  $a = -0.40$ ,  $b = 81.43$ . For mouse dataset, the parameters value are  $a = -0.35$  and  $b = 75.75$ . The variation in accuracy influences the integration strategy, which will be discussed in Section III-B3.

An example of the forces landscape and the prediction completion level result when  $\Delta t = 0$  is shown in Fig. 10-(b).

The output of the LSTM-RNN is a vector  $c_{\text{force}}$  with size of  $1 \times K$  and each element value refer the completion level from time  $t$  to  $t+k$  in the future.

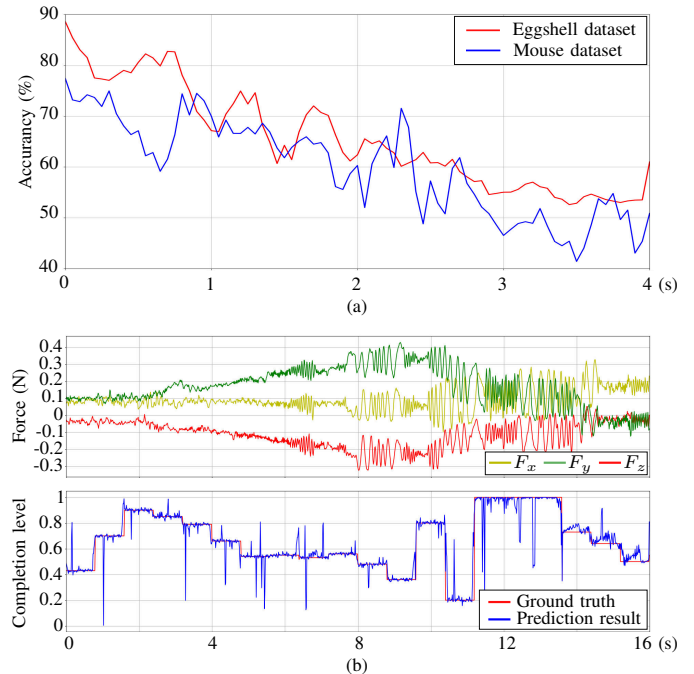


Fig. 10. Training results of the LSTM-RNN. (a) The image of the change in accuracies of drilling completion level recognition  $acc(\Delta t)$  with  $\Delta t$  for eggshell dataset (red line) and mouse dataset (blue line) based on data from time  $t-l$  to  $t$ ; (b) Forces landscape and the prediction result at time  $t$  within a drilling turn.

*3) Completion level results integration:* In Section III-B1 and Section III-B2, the drilling completion levels were independently estimated based on image and force information, albeit at different temporal and spatial scales. The advantage of recognition based on image processing is that the image taken by the upper camera provides single-shot drilling completion level of all points in the trajectory, while the disadvantages are relatively low spatial resolution and occlusion issues. On the other hand, the recognition module based on force sensor can predict the instantaneous changes in completion level of the contact area at the current moment with high accuracy without occlusion issues, but has little global prediction power besides a close future. In order to make good use of the advantages of both sensors, in this work we propose an integration strategy.

*a) Temporal synchronization:* In our system, the acquisition, distribution, and communication of data from various sensors are facilitated by ROS Noetic Ninjemys, which includes an advanced message synchronization component designed to handle temporal inconsistencies in sensor fusion [37]. As a result, the synchronization of timestamps between received images from 4K camera and information from force sensor can be easily accomplished. However, the different number of trajectory measure points caused by different frequencies of sensors is still required for harmonization.



The output of the image-based completion level recognition part is a vector  $\mathbf{c}_{\text{image}}$  with size of  $1 \times m$ , where  $m = 32$  is the number of measure points along the trajectory, while the output of the force-based part is a vector  $\mathbf{c}_{\text{force}}$  with size of  $1 \times K$ , where  $K = 80$  is the sample size of predicted points. The predicted area for force processing network is set to be a quarter of a whole circle, which refers to the sample size of the whole drilling trajectory points will be 320. Considering upsampling to a higher frequency helps to preserve more information and reduce the risk of losing critical data, we use nearest-neighbor interpolation of  $\mathbf{c}_{\text{image}}$  to a new vector  $\mathbf{c}'_{\text{image}}$  with size of  $1 \times L$ ,  $L = 320$ .

b) *Spatial synchronization*: Because the force-based completion level prediction does not have global information, it does not know which point is being drilled. To empower it with that information we align it spatially with the image-obtained information. Each element of  $\mathbf{c}'_{\text{image}}$ ,  $c_{i,\text{image}}$ ,  $i = 1, \dots, L \in \mathbb{N}$ , reflects the completion level of the  $i$ -th measure point  $\mathbf{p}_i$  on the circular trajectory whose coordinate in the  $x$ - $y$  plane can be calculated as

$$p_{x,i} = \cos\left(\frac{i-1}{L} \cdot 2\pi\right), p_{y,i} = \sin\left(\frac{i-1}{L} \cdot 2\pi\right).$$

On the other hand, each element  $c_{j,\text{force}}$  of  $\mathbf{c}_{\text{force}}$ ,  $j = 1, \dots, K \in \mathbb{N}$ , reflect the completion level of the point that is the  $j$ -th point forward from the current point  $\mathbf{p}_{\text{current}}$  along the circular trajectory. The coordinate of  $\mathbf{p}_{\text{current}}$  can be read directly from the input of the LSTM-RNN (discussed in Section III-B2), which is denoted as  $x$  and  $y$ .

We apply least squares to find a  $i_0$  ensuring the point  $\mathbf{p}_{i_0}$  is the closest point to  $\mathbf{p}_{\text{current}}$ , and create a  $\mathbf{c}'_{\text{force}}$  with size of  $1 \times L$  whose element value is  $c'_{q,\text{force}}$  ( $q = 1, \dots, L \in \mathbb{N}$ ). If  $i_0 \leq L - K$ ,  $\mathbf{c}'_{q,\text{force}}$  can be calculated as:

$$c'_{q,\text{force}} = \begin{cases} c_{q-i_0,\text{force}} & i_0 < q \leq i_0 + K \\ 0 & \text{others} \end{cases}, \quad (20)$$

while if  $i_0 > L - K$ ,  $\mathbf{c}'_{q,\text{force}}$  can be calculated as:

$$c'_{q,\text{force}} = \begin{cases} c_{q-i_0,\text{force}} & i_0 < q \leq L \\ c_{q+L-i_0,\text{force}} & 0 < q \leq i_0 + K - L \\ 0 & \text{others} \end{cases}. \quad (21)$$

In this way, we have  $\mathbf{c}'_{\text{image}}$  and  $\mathbf{c}'_{\text{force}}$ , both of which have a size of  $1 \times L$  and each corresponding element reflects the recognition completion level of same measure point based on image and force, respectively.

c) *Information fusion*: It is necessary to reiterate that the main reason we want to fuse the recognition results by image and force is that the result by image of the area obscured by the drill cannot be updated, whereas the force information only gives expected completion level changes not absolute levels. Therefore the information obtained by the image can be used as the current recognition result of the unobscured areas, while the integrated sensorial information is used for the obscured areas.

Consider a vector of integration  $\mathbf{c}_{\text{inte}}$  with size of  $1 \times L$  can be calculated as:

$$\mathbf{c}_{\text{inte}}^T = \mathbf{W}_1 \mathbf{c}'_{\text{image}}^T + \mathbf{W}_2 \mathbf{c}'_{\text{force}}^T, \quad (22)$$

where  $\mathbf{W}_1$  and  $\mathbf{W}_2$  are the weighting matrix with size of  $l \times L$  of the recognition result by image and force, whose elements reflect the weight of both results based on the accuracy.

To simplify the calculation, we create two weights  $\mathbf{w}_1$  and  $\mathbf{w}_2$  with size of  $1 \times L$  whose element  $w_{r,1}$  and  $w_{r,2}$  ( $r = 1, \dots, L \in \mathbb{N}$ ) are the weight of the corresponding element  $c_{r,\text{image}}$  in  $\mathbf{c}'_{\text{image}}$  and  $c_{r,\text{force}}$  in  $\mathbf{c}'_{\text{force}}$ . The relationship between weighting matrix and weighting vector is

$$\mathbf{W}_1 = \text{diag}\{\mathbf{w}_1\}, \mathbf{W}_2 = \text{diag}\{\mathbf{w}_2\}, \quad (23)$$

where  $\text{diag}\{\}$  denotes a diagonal matrix.

The accuracy of the recognition result by force can be calculated using (19). Thus, similar to (20) and (21), the nearest measure point is numbered  $i_0$ , and  $w_{r,2}$  can be calculated if  $i_0 \leq L - K$  as:

$$w_{r,2} = \begin{cases} (a(r-i_0)+b)/100 & i_0 < r \leq i_0 + K \\ 0 & \text{others} \end{cases},$$

and if  $i_0 > L - K$ ,

$$w_{r,2} = \begin{cases} (a(r-i_0)+b)/100 & i_0 < r \leq L \\ (a(r+L-i_0)+b)/100 & 0 < r \leq i_0 + K - L \\ 0 & \text{others} \end{cases}.$$

where  $a = -0.40$ ,  $b = 81.43$  for eggshell dataset and  $a = -0.35$ ,  $b = 75.75$  for mouse dataset.

Accordingly, because the recognition result by image at the area obscured is considered as invalid,  $w_{r,1}$  can be simply calculated as:

$$w_{r,1} = 1 - w_{r,2}.$$

Substituting the results of  $\mathbf{w}_1$  and  $\mathbf{w}_2$  into (23), we can obtain the weighting matrix  $\mathbf{W}_1$  and  $\mathbf{W}_2$ . Then substitute the result into (22), the integration result  $\mathbf{c}_{\text{inte}}$  can be calculated.

In conclusion, the integration result of completion level  $\mathbf{c}_{\text{inte}}$  using image-based recognition result and force-based recognition result is obtained, and will be applied to calculate the lowering velocity of drill by (1).

#### IV. EXPERIMENTS

In this study, we first added the plane fitting block and force-based completion level recognition part sequentially to the original system, and conducted several experiments on eggshell drilling to verify the validation of the two new parts on improving the success rate and shortening the drilling time with comparison to our former study. Then, we use the whole system to conduct an experiment on *postmortem* mouse skull drilling to validate its effectiveness.

##### A. System configuration

The experiments a software implementation on a Ubuntu 20.04 x64 system. The robotic arm is controlled as described in our previous work [1]. ROS Noetic Ninjemys was used for the interprocess communication and CoppeliaSim (Coppelia Robotics, Switzerland) for the simulations. Communication with the robot was enabled by the SmartArmStack<sup>4</sup>. The dual quaternion algebra and robot kinematics were implemented

<sup>4</sup><https://github.com/SmartArmStack>

using DQ Robotics [38] with Python3. The force sensor was connected to a Raspberry Pi 4 Model B and the force data was read at 128 samples per second (SPS) using Python’s SMBus module and an I2C analogue input board.

### B. Setup

The hardware part of the system is set up as shown in Fig. 1. A mouse or an egg is fixed stably using the clamping platform. Fig. 2 shows the clamping platform for mice used for the system of mouse skull drilling and Fig. 3 shows that for the system of eggshell drilling. For both systems, a micro drill is held by a robot arm and a 4K camera is set vertically above the center of the mouse or egg to observe the drilling procedure. Only for the system of eggshell drilling, an air compressor with a silicone tube is applied to blow away the shell dust emitted from drilling the surface of the eggshell. As for the pre-trained model of both image-based and force-based neural networks applied in the completion level recognition, eggshell network models trained under eggshell datasets are applied for the eggshell drilling system while mouse skull network models are applied for the mouse skull drilling system. Before the experiment starts, the drill is teleoperated by an operator to adjust the starting point so that it is within the field-of-view of the camera throughout the entire circular path. We planned the drilling trajectory with the method mentioned in Section III-A.

For software part of the system, we applied three different setups for different experiments summarized in Table II. Setup 1 is the same as our former study with only image-based completion level recognition and serves as comparison group to other two setups. Setup 2 adds the plane fitting block to setup 1, and setup 3 adds the force-based completion level recognition part to setup 2. Also, setup 3 is applied for mouse skull drilling experiment for a final evaluation.

TABLE II  
THE SETUPS IN DIFFERENT EXPERIMENTS.

	Image-based	Plane fitting	Force-based
Setup 1 [8]	√	×	×
Setup 2 [Proposed]	√	√	×
Setup 3 [Proposed]	√	√	√

TABLE III  
THE PARAMETERS DURING THE EXPERIMENTS.

Parameters	$v_z$ (m/s)	$r$ (mm)	$f$ (Hz)
Selected value	$-6 \times 10^{-6}$	4	30

### C. Preparation

The parameters used in the experiments, namely the initial speed  $v_z$  of the drill in (1), the radius of the circular drilling path  $r$ , and the frequency  $f$  of the transmission of the calculated  $z$ -positions to the robot are summarized in Table III. Also, the drilling will stop autonomously when the system judges the drilling procedure as complete. This happens when 80% of the points on the drilling path achieve at least 0.85 of completion level.

### D. Experiment 1: validation of the plane fitting block on eggshell

With setup 2, we performed a total of 20 trials with 20 different eggs of random shape, size, and thickness of shell to verify the validation of the plane fitting block. After the autonomous drilling algorithm stopped, we tried to remove the resected circular shell piece manually using tweezers. If the eggshell could be removed without damaging the membrane beneath the eggshell, the experiment was deemed successful. On the other hand, if the membrane broke during the drilling or removal procedure, or the eggshell was not easily removed, the experiment was counted as a failure. If the robot over-drilled the egg and ruptured the membrane, this would also be considered a failure.

The comparison group is the result of 20 trials using the robotic drilling system without the plane fitting block (setup 1), which was conducted in our former research [8] (result shown in Fig. 13). The success rate and total drilling time are recorded and compared between experimental group and two comparison groups.

1) *Results and discussion:* In the experiment, 17 out of 20 cases were successful, resulting in a success ratio of 85% (shown in Fig. 13). The average required time for successful drilling was 8.0 min.

Compared to the system without any plane fitting (80% success rate and 16.8 min average drilling time), it can be concluded that the plane fitting improves the success rate and drilling speed in eggshells. This suggests that the long drilling time and failure caused by the tilted initial pose of the egg in our former research was overcome by the plane fitting.

Errors in completion level recognition can be the reason for all the 3 failure cases in experimental group, one of which is shown in Fig. 11-(a). One screenshot before the membrane was ruptured by the drill is also shown in Fig. 11-(b). We can see that the upper part of the trajectory is 100% drilled so the correct completion level recognition result of that area should be 1. However, the recognition result from the neural network was less than 1, as shown in Fig. 11-(c), directly resulting in the membrane rupture. That refers the recognition accuracy of the neural network limited the upper limit of the success rate for the eggshell drilling procedure and refining the neural network for a higher recognition accuracy or adding additional sensors to help the image processing is necessary in the future work.

### E. Experiment 2: validation of the force-based completion level recognition on eggshell

Similar to experiment 1, we performed a total of 20 trials on eggshells with setup 3 to verify the validation of the force-based completion level recognition. The success rate and average time is calculated after the experiment.

1) *Results and discussion:* The success rate of the experiment with setup 3 is 95% (19 out of 20 cases). The average duration for successful drilling was 7.1 min. The result is also shown in Fig. 13. The increase in accuracy and shortening of drilling time are in line with expectations because with the force data, the lag during completion level

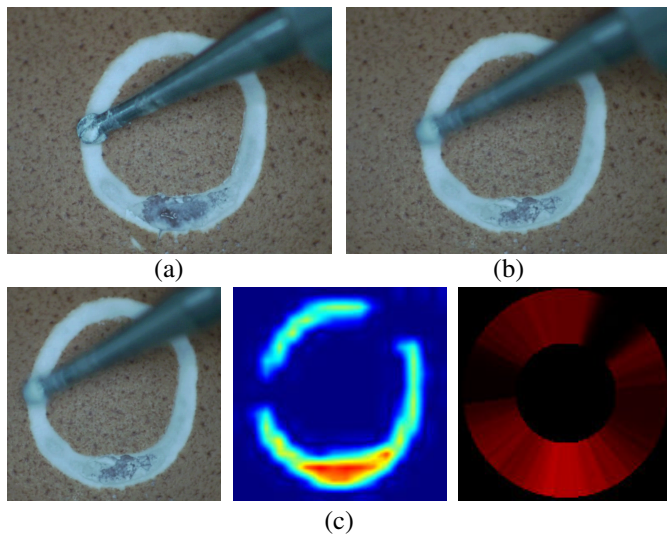


Fig. 11. (a) A failure case of experiment 1 caused by recognition errors of completion level; (b) The screenshot before the moment that the rotating drill damaged the membrane; (c) The recognition result (cropped image from bounding box detection, heatmap of the completion level map and progress bar) of the screenshot.

updating will be eliminated and the recognition results of completion level of contact point that is about to be penetrated are more accurate, which prevent the drill from going down continuously breaking the membrane. As a result, it can be concluded that with the integration of the force data, the success rate and drilling speed improves in eggshell drilling.

The only failure case is shown in Fig. 12-(a). The reason of the failure is that the drilling stopped automatically because 80% of points on the drilling path achieve at least 0.85, which is the conditions of drilling completion (described in Section IV-C), but the eggshell inside the drilling area could not be removed by tweezers manually. The integration result of the completion level estimated by image and force is shown in Fig. 12-(b). We can see that almost all the areas except the upper right part of the trajectory is 100% drilled. However, even if the portion that is not thoroughly penetrated is only a small portion, it still may have a significant impact on removing the entire eggshell. That refers the stop criteria might need to be reconsidered in the future work.

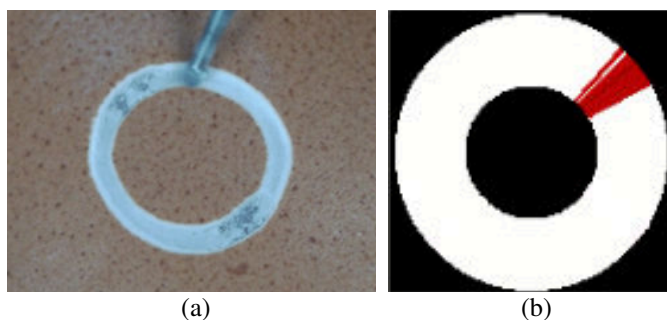


Fig. 12. (a) The failure case of the experiment 2 caused by the stop criteria; (b) The progress bar that is generated based on the integration result of image processing and force data.

### F. Experiment 3: validation experiment on postmortem mouse skull

Even though the autonomous drilling system with plane fitting works well on eggshells, it is still necessary to verify the feasibility on mouse skull drilling. 20 trials with skull drilling on 20 different *postmortem* mice were conducted. Similarly to the eggshell experiment, the resected circular mouse skull patch being easily removable manually with tweezers defined successes and failures.

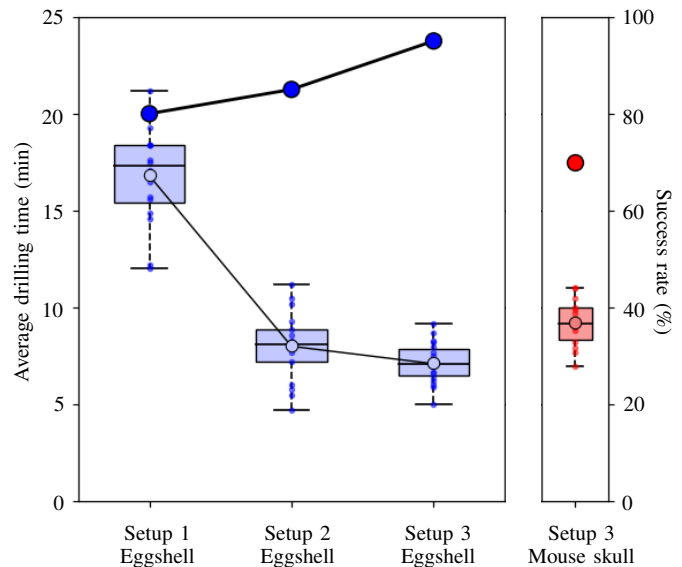


Fig. 13. Comparison of the results for all setups. The box plot represents the average drilling time with different setups while the point chart represents the success rate. The left three bars are the results of eggshell drilling with setup 1 to 3, and the line chart shows the trend of success rate and drilling time with the change of setups. The right bar is the result of mouse skull drilling with setup 3.

1) *Results and discussion:* In the experiment, 14 out of 20 cases were successful, resulting in a success ratio of 70%. The average required time for successful drilling was 9.3 min. The result of *postmortem* mouse skull drilling is also shown in Fig. 13. A typical case of success is shown in Fig. 14. In the case, the drilling procedure stopped automatically when it was judged as complete and the circular patch was removed perfectly. We can conclude that the system effective for mouse skull drilling with a considerable success rate and drilling speed.

Five out of six of the failure cases were caused by the wrong recognition result of the completion level, which is understandably less accurate than eggshell drilling given the more complex image and material. For image-based recognition, one main reason is considered to be that the color change of the drilling areas of the mouse skull is much less visible than those of eggshells. The color of eggshells change from brown to white to gray with the drilling completion level growth, making it relatively easier for neural network. However, the color change of mouse skull is not only related to the completion degree of drilling, but also the individual differences in mice, surface humidity of skull, the time period between euthanasia and experiment and so on, which lead to



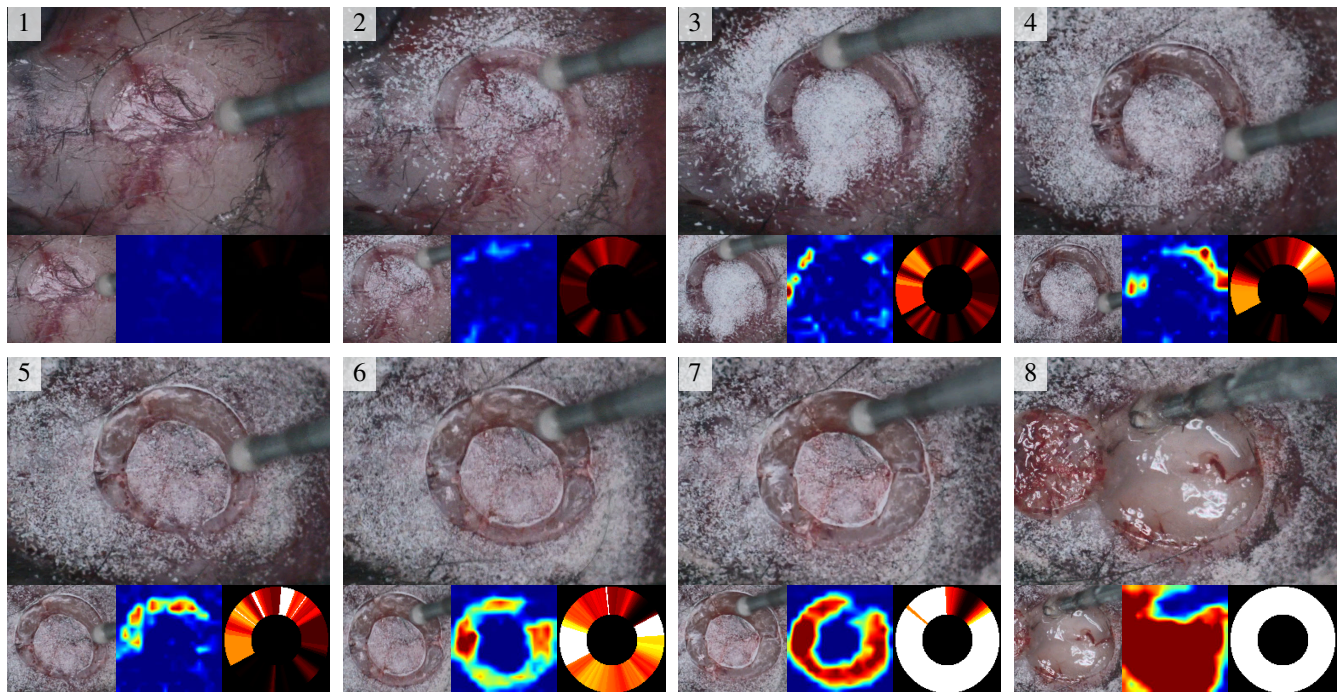


Fig. 14. A series of snapshots of a case of success drilling on *postmortem* mouse skull from the start of drilling to the removal of resected circular shell piece. Original image, cropped image, heatmap (generated by image processing) and drilling progress bar (generated based on the estimation result of both image and force) are shown for each snapshot.

the difficulties of recognition. For example, if the experiment is conducted soon after the euthanasia and the skull is relatively moist, the color will not change a lot during drilling. On the other hand, if the experiment was conducted long after the euthanasia, the skull will become dry and the color will be whiter as the drilling completion level grows. Also, the degree of moistness will also have influence on the stiffness of the skull, leading to wrong results in the force-based recognition. The accuracy of force-based recognition will also be influenced by the exudation of fluids. In several trials, bleeding occurred during the drilling process resulting in the stiffness and color of the drilling area changing, therefore the recognition result was negatively affected. Other reasons such as the reflected light from wet surface of mouse skull also negatively influenced the results.

More complex models of neural network for both image-based and force-based recognition more robust to the color or moistness change can help to some extent but processing speed can suffer. Additional sources of information, such as audio or vibration, can be added in future work to improve robustness.

## V. CONCLUSION

In this paper, we proposed a autonomous robotic drilling system for cranial window creation. To achieve this, a trajectory planner that can adapt to the plane to be drilled and avoid overshoot is imposed, and a plane fitting method is added to solve the problem caused by long drilling time. In order to adjust the generated trajectory in real-time, we applied neural networks to recognize the completion level of drilling based on image and force data obtained during drilling procedure

in real-time. In the experiment, we showed that our robotic drilling system is able to achieve a considerable success rate and speed in the procedure of autonomous drilling with an egg model and demonstrates the possibility of the system on mice cranial window creation procedure.

Future works include enhancing the robustness of the completion level recognition block by fine-tuning the neural network, considering a more accurate and objective drilling stop criteria, and improving the success rate of drilling by further including multimodal information such as audio wave to achieve the ultimate goal of cranial window creation on anesthetized live mice.

## REFERENCES

- [1] M. M. Marinho, J. J. Quiroz-Omaña, and K. Harada, "A multiarm robotic platform for scientific exploration: Its design, digital twins, and validation," *IEEE Robotics & Automation Magazine*, pp. 2–12, 2024.
- [2] H. Koike, K. Iwasawa, R. Ouchi, M. Maezawa, K. Giesbrecht, N. Saiki, A. Ferguson, M. Kimura, W. L. Thompson, J. M. Wells, A. M. Zorn, and T. Takebe, "Modelling human hepato-biliary-pancreatic organogenesis from the foregut–midgut boundary," *Nature*, vol. 574, no. 7776, pp. 112–116, sep 2019.
- [3] P. T. Ly, A. Lucas, S. H. Pun, A. Dondzillo, C. Liu, A. Klug, and T. C. Lei, "Robotic stereotaxic system based on 3d skull reconstruction to improve surgical accuracy and speed," jan 2020.
- [4] L. Ghanbari, M. L. Rynes, J. Hu, D. S. Schulman, G. W. Johnson, M. Laroque, G. M. Shull, and S. B. Kodandaramaiah, "Craniobot: A computer numerical controlled robot for cranial microsurgeries," *Scientific Reports*, vol. 9, no. 1, jan 2019.
- [5] N. Pak, J. H. Siegle, J. P. Kinney, D. J. Denman, T. J. Blanche, and E. S. Boyden, "Closed-loop, ultraprecise, automated craniotomies," *Journal of Neurophysiology*, vol. 113, no. 10, pp. 3943–3953, jun 2015.
- [6] L. Andreoli, H. Simplicio, and E. Morya, "Egg model training protocol for stereotaxic neurosurgery and microelectrode implantation," *World Neurosurgery*, vol. 111, pp. 243–250, 2018.

- [7] T. Okuda, K. Kataoka, and A. Kato, "Training in endoscopic endonasal transphenoidal surgery using a skull model and eggs," *Acta neurochirurgica*, vol. 152, pp. 1801–1804, 2010.
- [8] E. Zhao, M. M. Marinho, and K. Harada, "Autonomous robotic drilling system for mice cranial window creation: An evaluation with an egg model," in *2023 IEEE/RSJ International Conference on Intelligent Robots and Systems (IROS)*. IEEE, 2023, pp. 4592–4599.
- [9] Y. Hu, H. Jin, L. Zhang, P. Zhang, and J. Zhang, "State recognition of pedicle drilling with force sensing in a robotic spinal surgical system," *IEEE/ASME Transactions on Mechatronics*, vol. 19, no. 1, pp. 357–365, feb 2014.
- [10] P. Loschak, K. Xiao, H. Pei, S. Kesner, C. Walsh, and A. Thomas, "Cranial drilling tool with retracting drill bit upon skull penetration," *Journal of Medical Devices*, vol. 6, p. 017522, 03 2012.
- [11] Y. Dai, Y. Xue, and J. Zhang, "Drilling electrode for real-time measurement of electrical impedance in bone tissues," *Annals of Biomedical Engineering*, vol. 42, no. 3, pp. 579–588, nov 2013.
- [12] —, "Vibration-based milling condition monitoring in robot-assisted spine surgery," *IEEE/ASME Transactions on Mechatronics*, vol. 20, no. 6, pp. 3028–3039, dec 2015.
- [13] Z. Ying, L. Shu, and N. Sugita, "Autonomous penetration perception for bone cutting during laminectomy," in *2020 8th IEEE RAS/EMBS International Conference for Biomedical Robotics and Biomechanics (BioRob)*. IEEE, nov 2020.
- [14] B. M. Pohl, A. Schumacher, and U. G. Hofmann, "Towards an automated, minimal invasive, precision craniotomy on small animals," in *2011 5th International IEEE/EMBS Conference on Neural Engineering*. IEEE, apr 2011.
- [15] D. C. Jeong, P. S. Tsai, and D. Kleinfeld, "All-optical osteotomy to create windows for transcranial imaging in mice," *Optics Express*, vol. 21, no. 20, p. 23160, Sep. 2013.
- [16] S. Hasegawa, K. Okada, and M. Inaba, "Vibration Recognition Learning System using Force and Sound Sensing integratively for Mouse Cranium Cutting in Cranial Window Surgery," in *2023 JSME Conference on Robotics and Mechatronics*, Nagoya, Japan, 2023.
- [17] Y. Jia, P. M. Uriguen Eljuri, and T. Taniguchi, "A bayesian reinforcement learning method for periodic robotic control under significant uncertainty," in *2023 IEEE/RSJ International Conference on Intelligent Robots and Systems (IROS)*. IEEE, Oct. 2023.
- [18] N. Dvornik, K. Shmelkov, J. Mairal, and C. Schmid, "Blitznet: A real-time deep network for scene understanding," 2017.
- [19] R. Girshick, "Fast r-cnn," 2015.
- [20] S. Ren, K. He, R. Girshick, and J. Sun, "Faster r-cnn: Towards real-time object detection with region proposal networks," 2015.
- [21] K. He, G. Gkioxari, P. Dollár, and R. Girshick, "Mask r-cnn," 2017.
- [22] W. Liu, D. Anguelov, D. Erhan, C. Szegedy, S. Reed, C.-Y. Fu, and A. C. Berg, "Ssd: Single shot multibox detector," 2015.
- [23] C.-Y. Fu, W. Liu, A. Ranga, A. Tyagi, and A. C. Berg, "Dssd : Deconvolutional single shot detector," 2017.
- [24] K. Simonyan and A. Zisserman, "Very deep convolutional networks for large-scale image recognition," 2014.
- [25] H. Noh, S. Hong, and B. Han, "Learning deconvolution network for semantic segmentation," 2015.
- [26] I. Kokkinos, "Ubernet: Training a 'universal' convolutional neural network for low-, mid-, and high-level vision using diverse datasets and limited memory," 2016.
- [27] A. Tokgoz and G. Unal, "A rnn based time series approach for forecasting turkish electricity load," in *2018 26th Signal Processing and Communications Applications Conference (SIU)*. IEEE, May 2018.
- [28] Y. Qin, D. Song, H. Chen, W. Cheng, G. Jiang, and G. W. Cottrell, "A dual-stage attention-based recurrent neural network for time series prediction," *CoRR*, vol. abs/1704.02971, 2017. [Online]. Available: <http://arxiv.org/abs/1704.02971>
- [29] S. Hochreiter and J. Schmidhuber, "Long short-term memory," *Neural computation*, vol. 9, no. 8, pp. 1735–1780, 1997.
- [30] Z. C. Lipton, D. C. Kale, C. Elkan, and R. Wetzell, "Learning to diagnose with lstm recurrent neural networks," 2015.
- [31] M. F. Stollenga, W. Byeon, M. Liwicki, and J. Schmidhuber, "Parallel multi-dimensional lstm, with application to fast biomedical volumetric image segmentation," *Advances in neural information processing systems*, vol. 28, 2015.
- [32] M. Sundermeyer, R. Schlüter, and H. Ney, "Lstm neural networks for language modeling," in *Thirteenth annual conference of the international speech communication association*, 2012.
- [33] Q. Liu, Y. Dai, M. Li, B. Yao, Y. Xin, and J. Zhang, "Real-time processing of force sensor signals based on lstm-rnn," in *2022 IEEE International Conference on Robotics and Biomimetics (ROBIO)*. IEEE, Dec. 2022.
- [34] F. Delorme *et al.*, "Butt-jointed DBR laser with 15 nm tunability grown in three MOVPE steps," *Electron. Lett.*, vol. 31, no. 15, pp. 1244–1245, 1995.
- [35] C. Kruger, "Constrained cubic spline interpolation," *Chemical Engineering Applications*, vol. 1, no. 1, 2003.
- [36] C. He, N. Patel, A. Ebrahimi, M. Kobilarov, and I. Iordachita, "Preliminary study of an rnn-based active interventional robotic system (airs) in retinal microsurgery," *International Journal of Computer Assisted Radiology and Surgery*, vol. 14, no. 6, pp. 945–954, Mar. 2019.
- [37] R. Li, Z. Dong, J.-M. Wu, C. J. Xue, and N. Guan, "Modeling and property analysis of the message synchronization policy in ros," in *2023 IEEE International Conference on Mobility, Operations, Services and Technologies (MOST)*. IEEE, May 2023.
- [38] B. V. Adorno and M. M. Marinho, "DQ Robotics: a library for robot modeling and control," *IEEE Robotics and Automation Magazine (RAM)*, vol. 28, no. 3, pp. 102–116, Sep. 2021, invited for presentation at IROS'21. [Online]. Available: <https://arxiv.org/pdf/1910.11612>